IEEE Photonics Journal
An IEEE Photonics Society Publication

Open Access

System Design and Performance Characterization of a MEMS-Based Laser Scanning Time-of-Flight Sensor Based on a 256 × 64-pixel Single-Photon Imager

Volume 5, Number 2, April 2013

Kota Ito
Cristiano Niclass
Isao Aoyagi
Hiroyuki Matsubara
Mineki Soga
Satoru Kato
Mitsutoshi Maeda
Manabu Kagami

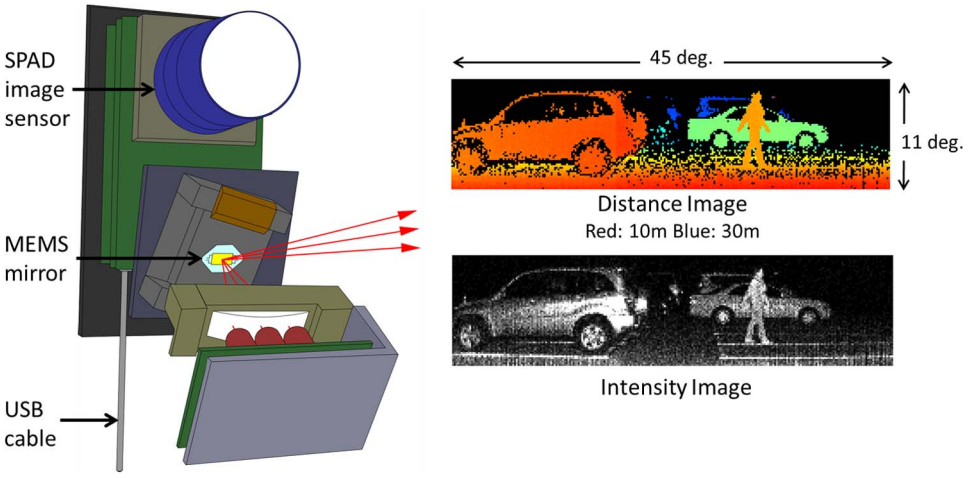

DOI: 10.1109/JPHOT.2013.2247586
1943-0655/$31.00 ©2013 IEEE

IEEE photonics SOCIETY

IEEE

System Design and Performance Characterization of a MEMS-Based Laser Scanning Time-of-Flight Sensor Based on a 256 × 64-pixel Single-Photon Imager

Kota Ito, Cristiano Niclass, Isao Aoyagi, Hiroyuki Matsubara, Mineki Soga, Satoru Kato, Mitsutoshi Maeda, and Manabu Kagami

Applied Optics Lab., Toyota Central R&D Labs., Inc., Nagakute 480-1192, Japan

DOI: 10.1109/JPHOT.2013.2247586

Manuscript received January 11, 2013; accepted February 11, 2013. Date of publication February 26, 2013; date of current version March 1, 2013. Corresponding author: K. Ito (e-mail: kotaito@mosk.tytlabs.co.jp).

Abstract: This paper reports on a light detection and ranging (LIDAR) system that incorporates a microelectromechanical-system (MEMS) mirror scanner and a single-photon imager. The proposed architecture enables a high signal-to-background ratio due to pixel-level synchronization of the single-photon imager and the MEMS mirror. It also allows the receiving optics to feature a large aperture, yet utilizing a small MEMS device. The MEMS actuator achieves a mechanical scanning amplitude of $\pm 4^\circ$ horizontally and $\pm 3^\circ$ vertically, while the field of view of the overall sensor is 45 by 11°. Distance images were acquired outdoors in order to qualitatively evaluate our sensor imaging capabilities. Quantitative ranging performance characterization carried out under 10 klx of ambient light revealed a precision of 14.5 cm throughout the distance range to 25 m, thus leading to a relative precision of 0.58%.

Index Terms: Three-dimensional image acquisition, laser range finder, light detection and ranging (LIDAR), mirror system design, quantum detectors.

1. Introduction

With the emerging need for high-resolution light detection and ranging (LIDAR) technologies in advanced driving assistance systems (ADASs), we have recently introduced a new concept of imaging time-of-flight (TOF) sensors that take advantage of a microelectromechanical-system (MEMS) scanner approach [1]. This paper focuses on the system design aspects of the proposed sensor and completes the previous paper with extended performance evaluation results.

While early concepts of MEMS scanner-based LIDAR sensors have been reported [2]–[4], a key advantage of our approach over previous implementations is the ability to operate each imaging pixel with a high signal-to-background light ratio (SBR) yet employing a small-area MEMS mirror. A high SBR requirement is important to extend the sensor operation to fully uncontrolled environments, such as under strong solar background light—a major challenge to most active near-infrared (NIR) depth sensors. In our approach, the MEMS mirror is only involved in the transmitting optical path, and hence, a MEMS mirror small enough to just accommodate the collimated laser beams may be effectively utilized. In the receiving path, we take advantage of a standard imaging lens and a 256 × 64 pixel image sensor whose pixels are actively gated in synchronization with the laser scanning pattern. Because of this synchronized gating approach, the individual pixels on the image

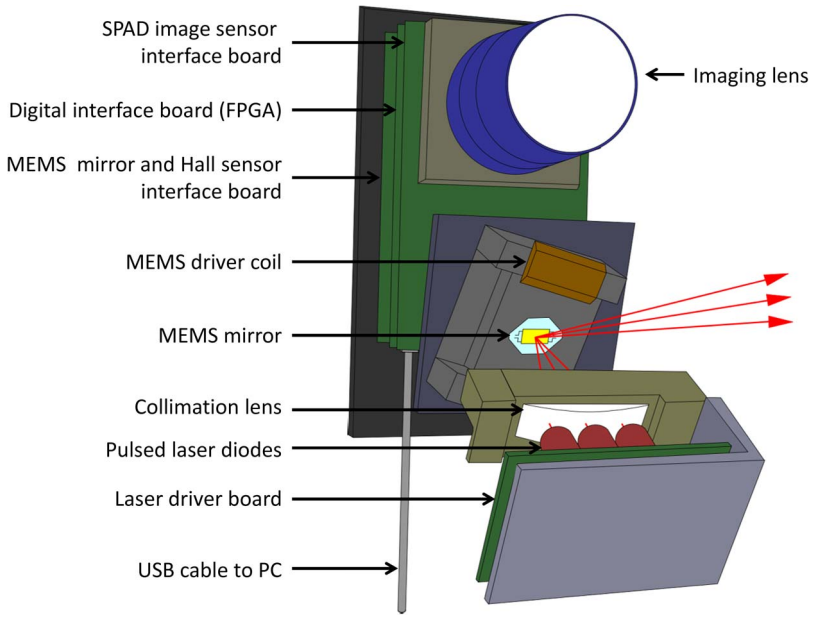

Fig. 1. Construction of the proposed LIDAR.

sensor do not integrate any background light when their corresponding points imaged on the target surface are not illuminated by the laser beam. In addition, since the imaging lens may be chosen arbitrarily, large aperture and small size lenses may be effectively employed. These advantages are enabled by the proposed image sensor architecture, which, in turn, is almost exclusively made possible by the subnanosecond gating capability and the resilience against electronic noise of the single-photon avalanche diode (SPAD) pixels in CMOS technology. We believe that the proposed sensor concept presents a good tradeoff between high-performance scanning LIDARs [5], [6] and the so-called TOF 3-D image sensors [7]–[19] in terms of performance, compactness, and cost.

The paper is organized as follows: In the next section, we introduce our depth sensor architecture and cover the design of those system components that were not described in our previous paper; in Section 3, we report the experimental results of the system components, as well as a complete performance evaluation of the LIDAR system under several background-light conditions. In Section 4, we introduce a figure of merit (FoM) analysis and update a comparison table of our results to the existing state-of-the-art. The paper is then concluded in Section 5.

2. Depth Sensor Architecture

Fig. 1 shows the construction of the proposed LIDAR. The transmitter and receiver optics are fully separated in order to miniaturize the transmitting optics without impacting the receiving aperture. The transmitter comprises laser diodes (LDs) and a MEMS mirror. The light signal is emitted from three LDs to mitigate the requirements of the scanning amplitude of the MEMS mirror in the horizontal direction. Furthermore, since the LD beams are separated from one another, they cannot reach the eye of a potential user simultaneously, thus mitigating the constraints of eye safety. As a result, the overall illumination power in our concept can be significantly increased, yet it can provide the same level of eye safety as a single LD system.

The horizontal and vertical actuations of the MEMS mirror are independent for flexible synchronization, enabling quasi-raster scanning, so Lissajous scanning is avoided. The scanning frequencies in the horizontal and vertical directions are 5 Hz and 1.3 kHz, respectively.

The optical signals reflected by the target are collected by a conventional lens and imaged onto the pixel array area of the image sensor chip. The chip then outputs a digital word formed by the TOF of each detected photon, as well as the associated pixel coordinates. Although SPADs are

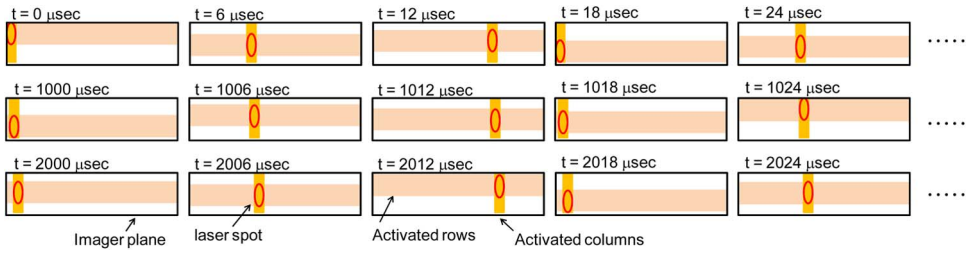

Fig. 2. Synchronization of MEMS mirror, the sensor chip, and the LDs.

sensitive to both signal and background photons, the use of statistical processing of the measured TOFs from repetitive laser pulses allows the signal to be discriminated from the background. This statistical processing for background rejection is commonly referred to as time-correlated single-photon counting (TCSPC). In TCSPC, a timing histogram is progressively built in a memory circuit by incrementing the bin at the memory address that is related to the TOF value of each detected photon. In the histogram, the timing position and amplitude of the resulting signal pulse are evaluated as a measure of the target distance and the signal intensity, respectively.

The synchronization of MEMS mirror, the sensor chip, and the LDs is designed to prevent background photons reflected on areas of the targets that are not illuminated by the LDs from being integrated in the TCSPC histogram, as illustrated in Fig. 2. The angle of the MEMS mirror and, hence, the direction of the LD beams are measured by Hall sensors. This information is then used to calculate the coordinates of the pixels on the focal plane where the LD signals are expected to reach. Vertical synchronization is then achieved by rejecting the TOF data from unilluminated pixel rows, while horizontal synchronization is achieved by activating only those columns that the LD signals are expected to reach. Furthermore, in order to optimally share row-level circuit resources, the three LDs emit pulses that are delayed with respect to each other.

Another advantage of our MEMS and image sensor synchronization approach is the reduction of the acquisition time of a given pixel, thus considerably reducing the impairment of distance measurement for nonstatic targets on that pixel, without the requirement for faster frame rates. In diffused light approaches, the acquisition time of a pixel is typically the inverse of the image sensor frame rate. As a result, motion artifact is addressed in those approaches by increasing the frame rate. However, as discussed in Section 4, the increase of the sensor frame rate has an impact on the sensor precision, unless the illumination power is increased by the same proportion. Our MEMS-scanning concept potentially mitigates this tradeoff relationship. Nevertheless, depending on its mirror size, the maximum achievable scanning frequency and, hence, frame rate of a MEMS-based sensor may be restricted to a smaller value than that achievable by the diffused light approach. In this paper, our sensor operates at 10 frames per second (fps).

2.1. MEMS Mirror

The MEMS mirror, whose design concept is reported in [20], was redesigned with new parameters in this paper. The mirror size is optimized to be relatively small but still sufficiently large to accommodate the LD beams. The mirror surface with dimensions of 4×8 mm^2 is gold plated to enhance the mirror reflectivity.

A moving magnet configuration was adopted to prevent the mirror plane from heating due to the driving currents. Four magnets are attached to the mirror surface, as shown in Fig. 3. The mirror tilts according to the force induced by the magnetic field of the driving coils. Unlike in [20], in order to reduce the system size in this paper, a single pair of driving coils enables 2-D scanning of the MEMS mirror. This is achieved by orienting the mirror to a nonorthogonal angle of 15° with respect to the coils and by superimposing the 5-Hz and 1.3-kHz current signals before injecting them into the coils. Furthermore, optical leveraging is utilized to achieve a FOV of 45 by 11° with relatively small MEMS tilting amplitudes. Optical leveraging is obtained by placing the LDs in a position as

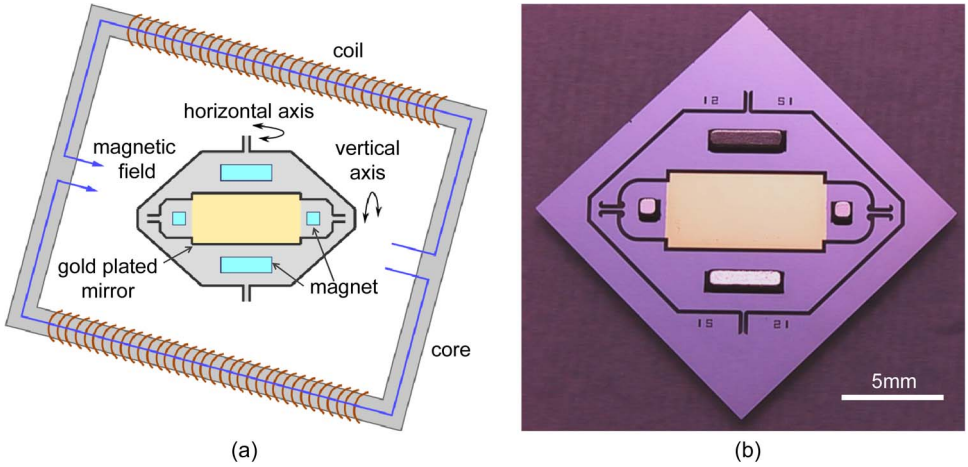

Fig. 3. Moving magnet type MEMS mirror. (a) Schematics with driving coil. (b) Manufactured device.

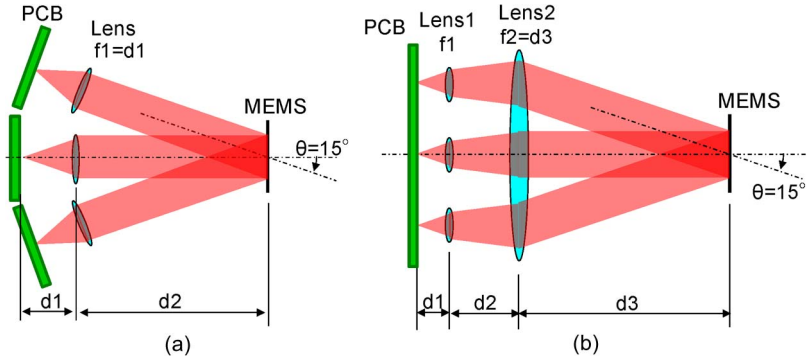

Fig. 4. Two candidates for the laser collimation optics: (a) Isolated collimation and (b) unified collimation.

close as possible to the normal to the mirror surface. As a result, the MEMS mirror tilting angles are limited to ± 4 and $\pm 3^{\circ}$ horizontally and vertically, respectively.

The output of the Hall sensors tracks their distance with respect to the magnets on the MEMS mirror. The signals are read by analog-to-digital converters (ADCs) on the MEMS driver board and are then sent to an FPGA for synchronization between the MEMS mirror and the image sensor. The relationship between the output of the Hall sensor and the angle of the MEMS mirror was characterized prior to its use in the LIDAR system.

2.2. Laser Collimation Optics

Compactness, ease of alignment, and low aberration were all taken into consideration for the design of the laser collimation optics. Two alignment architectures were compared, as depicted in Fig. 4. In the first architecture, referred to as "isolated collimation," three printed-circuit boards (PCBs) set at different angles are utilized, and individual collimation lenses for each LD are attached onto each PCB. In the second architecture, here referred to as "unified collimation," the beams of three LDs that are placed on the same PCB are collected by one additional larger lens. Collimation is achieved by both the small and large lenses. In the case of isolated collimation, optical design is relatively flexible because only one collimation lens is required. However, the alignment of three PCB boards adds complexity to the mechanical design and assembly. Optical design in the case of unified collimation is more complex, but its mechanical alignment is easier

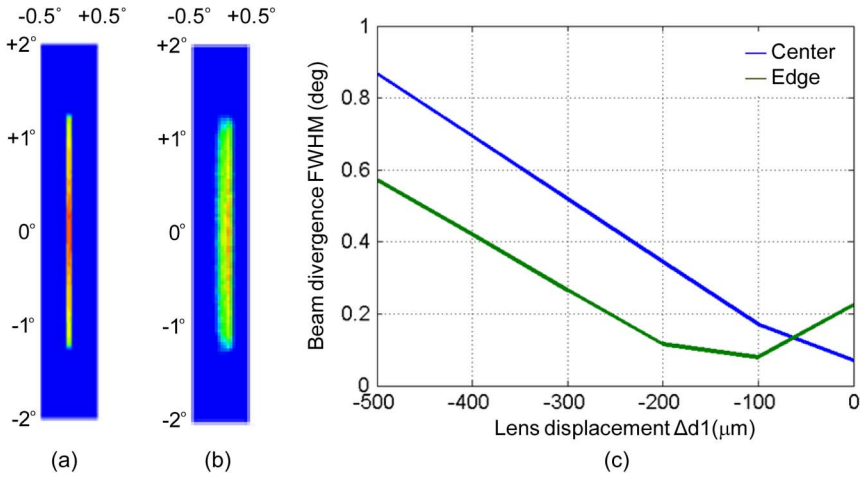

Fig. 5. Laser aberration. (a) Center laser beam spot. (b) Edge laser beam spot. (c) Relationship between d1 and the horizontal divergence.

than that required for isolated collimation. We have opted for the unified collimation approach in this paper.

The aspect ratio of the laser beam is approximately 1 : 12, which is determined by the shape of the emission aperture of the LD. In order to illuminate a small number of columns on the image sensor, the laser beams are oriented with their larger divergence angles along the vertical axis. The simulated beam aberrations of the center and the edge LDs at position d1 of the best collimation position d1,0 for the center LD beam are shown in Fig. 5. In the vertical direction, both results show the same divergence of 2.4° full width at half-maximum (FWHM). On the other hand, the horizontal divergences are different, i.e., 0.07° and 0.23° FWHM for the center and the edge LDs, respectively. The horizontal FWHM is simulated with several $\Delta d1 = d1 - d1, 0$, as shown in Fig. 5(c). As can be seen in Fig. 5(c), the horizontal divergence may be varied independently from 0.1° to 0.5° for each lens by carefully tuning $\Delta d1$. The smallest divergence angle is achieved at a $\Delta d1$ of approximately -100 μm for the edge LDs.

The collimated beam size, which imposes a limit on the miniaturization of the MEMS mirror size, is simulated and corroborated by analytical calculation. From the divergence angle of the LD and the focal length of the lenses, the beam size is calculated to be 1.7×3.5 mm^2 FWHM. Assuming an ideal reflectivity coefficient of 100% on the mirror surface, in order to reflect signal light with efficiency of more than 98%, a mirror aperture of 1.4 times the FWHM is theoretically required. The simulated reflection efficiency, i.e., the ratio of the reflected light to the incoming light, taking into account beam aberration is shown in Fig. 6. Reflection efficiencies better than 98% are achieved with a mirror size of 4×6 mm^2. The analytical calculation, in which aberration is not included, also corroborates this result. Note that additional losses due to the nonideal reflectivity of the gold-plated mirror surface are not included in this result. The mirror size is eventually designed to be 4×8 mm^2 to allow some margin for the alignment of the three laser beams.

2.3. Laser Driver

The simplified electrical schematics of the laser driver are shown in Fig. 7. For a short and high peak-power optical pulse, a high driving voltage is typically required due to the parasitic inductance L_1 that appears in series with the LD. This inductance induces a voltage drop upon fast current transitions, which reduces the effective voltage that is applied to the LD. Transient waveforms of the LD driver, simulated using a Spice simulator, are shown in Fig. 8. When M_1 turns on, V_A is pulled down from V_0 to 0 V. V_B, which is ac coupled to V_A, also makes a transition from 0 V to $-V_0$, as shown in Fig. 8(b). The current through L_1 recharges the capacitor C_1, which, in turn, reduces the voltage applied to L_1. The current slew rate of L_1 decreases accordingly. When V_B reaches 0 V

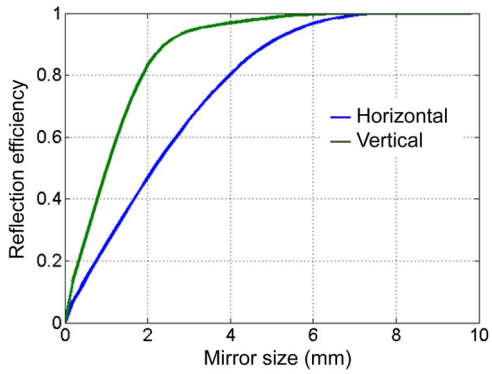

Fig. 6. Reflection efficiency as a function of the mirror size.

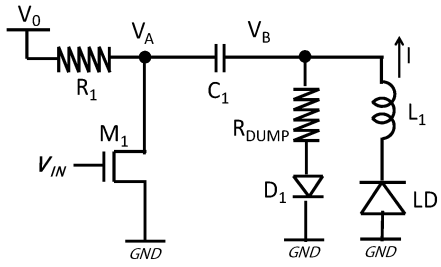

Fig. 7. Simplified electrical schematic of the laser driver.

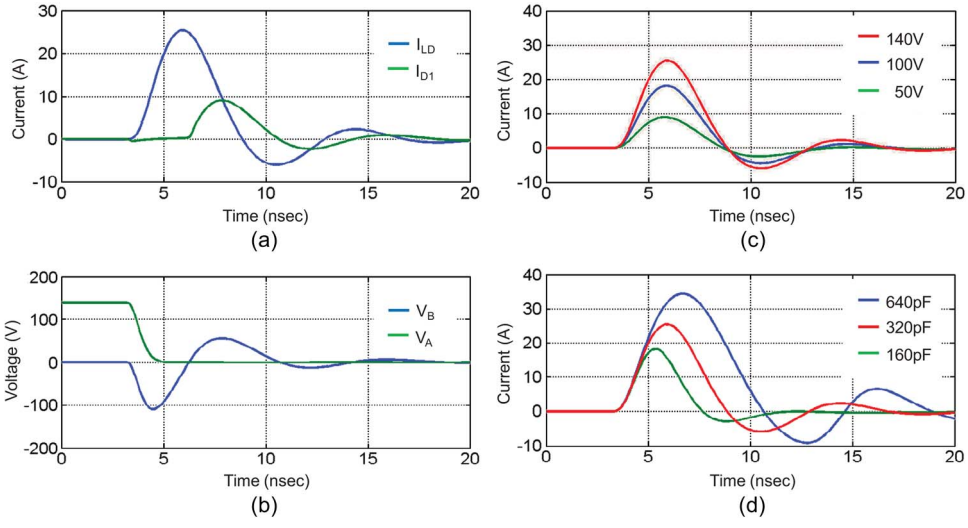

Fig. 8. Transient simulation results of the designed LD driver circuit. (a) Current. (b) Voltage. (c) I_{LD} for several values of V_0 with $C_1 = 320$ pF. (d) I_{LD} for several values of C_1 with $V_0 = 140$ V.

again, the current reaches its maximum value and subsequently starts decreasing because of the positive value of V_B. The falling edge is relatively slow due in part to the current through R_{DUMP} and diode D_1, which are added to avoid oscillation and reverse currents on the LD.

Since the LD, D_1, and the MOSFET M_1 are nonlinear devices, it is difficult to estimate the pulsewidth analytically. However, assuming a simple LC resonance circuit consisting of L_1 and C_1, we may explain the trend qualitatively. The peak value of the current pulse increases proportionally

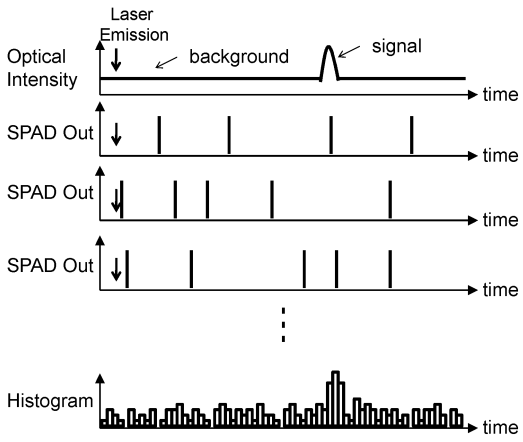

Fig. 9. TCSPC histogram.

to V_0 and C_1, while the pulse duration increases in proportion to C_1. In Fig. 8(c) and (d), simulation results for several values of V_0 and C_1 confirm these relationships.

Generally, V_0 is set as large as possible to obtain maximum amplitude; meanwhile, C_1 should be chosen as a compromise between the pulsewidth and the peak power. In our implementation, while V_0 of 140 V is set to satisfy the maximum voltage rating of M_1, a value of 320 pF is chosen for C_1 as the best compromise.

2.4. Signal Processing

TOF data from the image sensor are processed in the FPGA to determine the distance to the target based on TCSPC. An illustration of a TCSPC histogram acquisition routine is shown in Fig. 9. Segments of a SPAD output starting at the time of laser emission and depicted in different rows for each LD emission, illustrates the systematic arrival time of the signal photons, i.e., TOF, as opposed to the random arrival times of uncorrelated background photons. The signal photons therefore form a peak in the histogram, while the background photons tend to be uniformly distributed over all the histogram bins. In the signal processing, memory circuits are utilized to accommodate a histogram of 512 bins for each pixel. The TOF of each detected photon is utilized as the address signal of the memory in order to increment the bin located at the TOF position. By repeating this process, the signal pulse in the histogram may be discriminated from the other bins under relatively low values of SBR. The target distance is then obtained by finding the location of the histogram bin with the maximum value [21].

Data from the CMOS sensor comprise a 12-bit TOF word, an 8-bit binary pattern, which indicates at which columns photons were detected, and a validation bit utilized in the readout interface. Since the histogram size is limited to 512 bins, the TOF word is compressed by three bits before it is utilized as the address of the histogram bin to be incremented.

The repeated laser pulse emission and the single-photon counting technique enable us to reconstruct the shape and timing of the laser pulse while rejecting background light. The number of all the detected photons is also calculated by summing up all the histogram bin values, which gives a measure of the intensity of each pixel. This intensity information may be used, for instance, to discriminate road features and signs such as lane separation lines and pedestrian crossings.

3. Experimental Results

3.1. MEMS Mirror

A manufactured MEMS mirror was characterized in terms of its scanning amplitude. The horizontal axis was driven by a dc ranging from −500 mA to 500 mA. The obtained mechanical

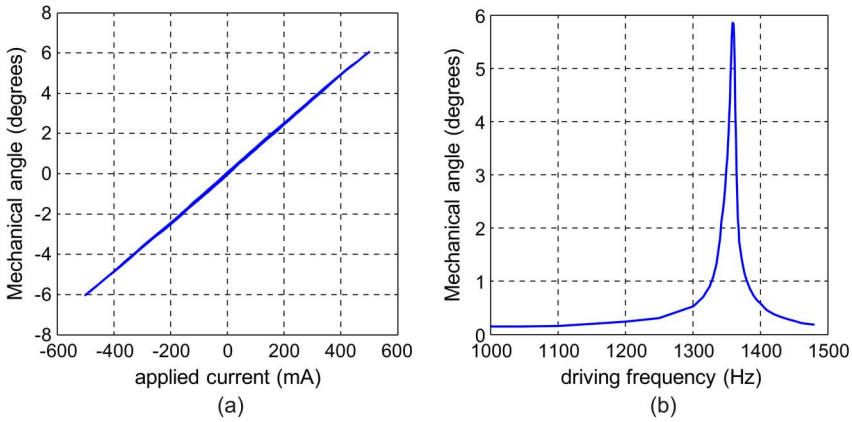

Fig. 10. Measured amplitude of MEMS mirror. (a) Horizontal axis. (b) Vertical axis.

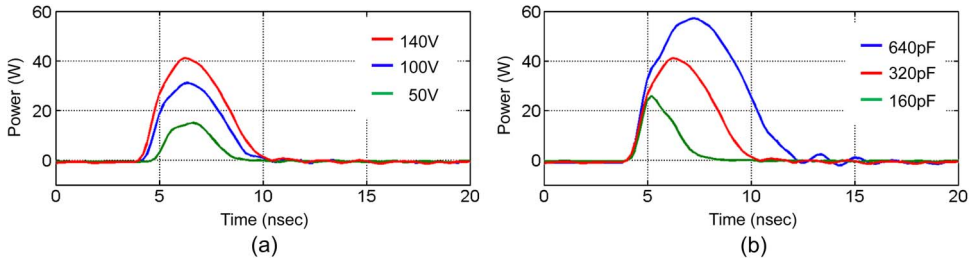

Fig. 11. Optical power for (a) several values of V_0 with $C_1 = 320$ pF. (b) Several values of C_1 with $V_0 = 140$ V.

angles are shown in Fig. 10(a), which reveals a maximum amplitude of $\pm 6^\circ$. Since hysteresis was negligible, control of the horizontal tilting angle of the MEMS mirror may be performed without the need for complex feedback circuits. The vertical axis was driven by a sine-wave signal with a 68 mA peak-to-peak current at various frequencies ranging from 1000 Hz to 1500 Hz. The maximum amplitude was obtained at 1359 Hz, which reaches 6°, as shown in Fig. 10(b). The amplitudes measured for both the horizontal and vertical axes therefore satisfied the required specifications of our LIDAR system.

3.2. Laser Driver

The implemented LD driver was characterized using a commercially available photodiode, an optical power meter, and a fast oscilloscope. The driver was characterized based on several values of V_0 and C_1, which were chosen to be the same as the simulated values in Fig. 8. The measured optical power waveforms are shown in Fig. 11. The obtained optical power was in agreement with the simulated transient currents in the LD. These results also supported the choice of V_0 of 140 V and C_1 of 320 pF as the best compromise between peak power and laser pulse duration. A peak power of 40 W and a pulse duration of 4 ns FWHM were achieved in the final implementation. In addition, the overall illumination power was increased for the final performance characterization by increasing the laser repetition rate from 300 kHz in [1] to 600 kHz.

3.3. LIDAR System

The assembly of the LIDAR system, illustrated in Fig. 1, led to an overall system size of $19 \times 15 \times 8$ cm^3, mainly due to the construction of the transmitting optics. We believe that a "folded optics" design is expected to considerably reduce the system size in the future. The TCSPC

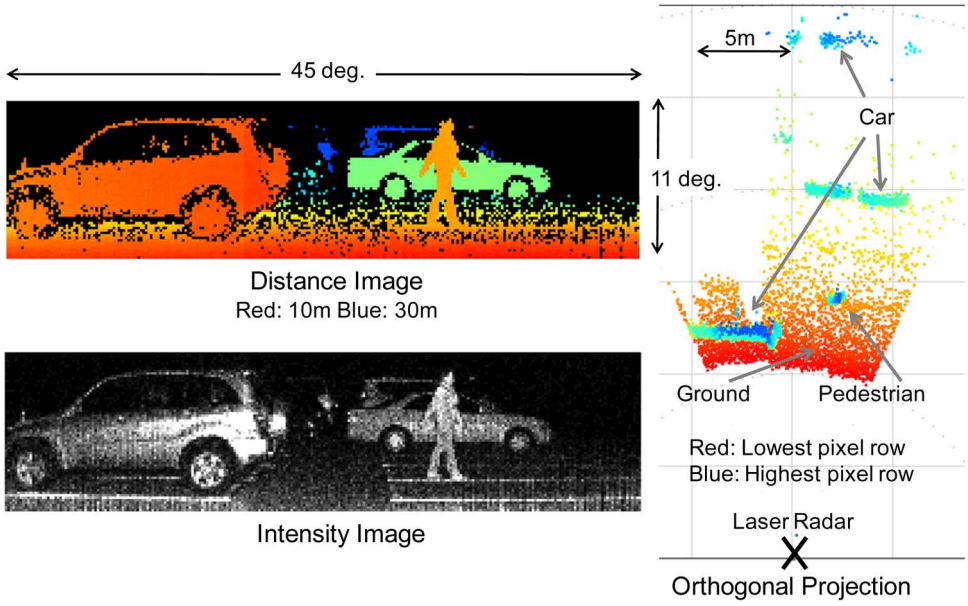

Fig. 12. Example of depth image and intensity acquired with the proposed sensor under low background illuminance.

algorithm was implemented on a low-cost FPGA, which also accommodated a soft-core microprocessor utilized to control the overall system. The sensor system was experimentally characterized in two ways. First, a qualitative characterization of the depth imaging was carried out to validate the system imaging capability. Then, a quantitative characterization of the ranging performance under various background conditions was performed to validate the immunity to background light, distance precision, and nonlinearity errors.

3.4. Depth Imaging

Depth images were acquired at 10 fps in several situations to check the overall sensor functionality. Fig. 12 shows one example of the acquired data, which was taken outdoors. In the distance image, the measured target distance is color-coded, red being close to the sensor and blue being far from the sensor. The shape of the pedestrian suggests the direction of future movement without requiring several additional frames. The car situated at a distance of 28 m from the sensor was successfully detected. No visible distortion was observed owing to the single-photon image sensor approach.

The number of photons, including signal and background light, is shown as a measure of brightness in the intensity image. Vertical fixed-pattern noise in the intensity image may be noticeable due to timing errors in the synchronization between the CMOS sensor and the MEMS driver.

In the orthogonal projection view, pixels are color coded according to their vertical position in the pixel array. The bottom pixel row is indicated as red, while the top pixel row is indicated as blue. The shapes and locations of two cars are imaged clearly. Data points on the ground were successfully imaged as a nearly continuous point cloud.

3.5. Performance Characterization

Ranging performance was quantitatively characterized within a distance range up to 25 m under several background light conditions. A wide board wrapped in a white cotton fabric was utilized as the target. It was placed in front of the sensor and moved from 2 m to 25 m in steps of 1 m. The distance between the sensor and the target was measured with a tape measure. At each distance, the measurement was repeated 100 times.

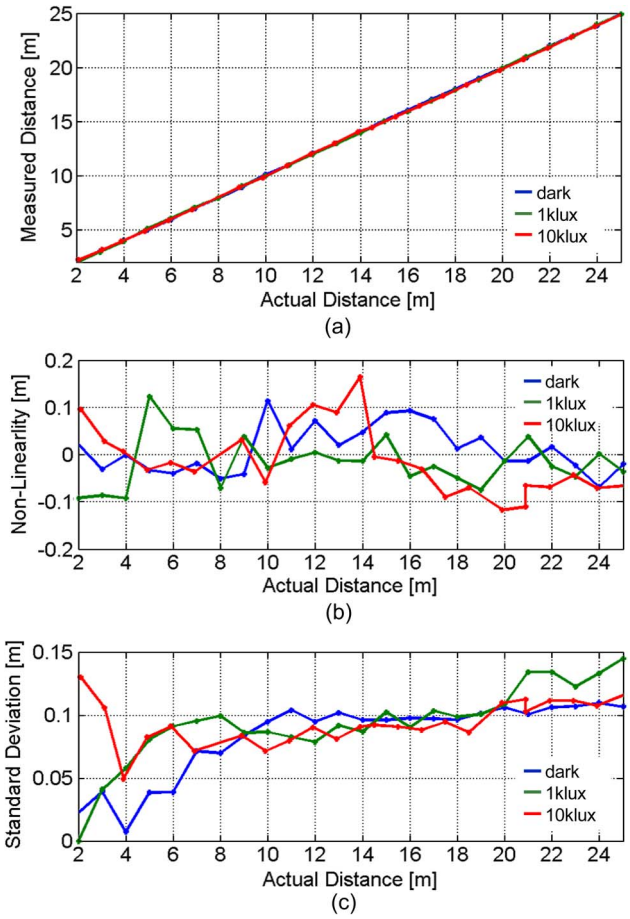

Fig. 13. Ranging performance. (a) Measured distance. (b) Nonlinearity error. (c) Standard deviation.

The mean value of each set of measured distances from one pixel is shown in Fig. 13(a). The nonlinearity error is calculated as the difference with respect to the ground truth values and is plotted in Fig. 13(b). The worst-case nonlinearity error, including the uncertainty on the measurement of the ground truth values, was less than 17 cm throughout the measurement range. The standard deviation was calculated using the same data and is shown in Fig. 13(c), for three conditions of background illuminance. Since the three results revealed approximately the same repeatability error, one may conclude that background illuminance up to 10 klx was fully rejected by our TCSPC processing, as well as by the synchronization between the sensor chip and the MEMS mirror. The worst-case standard deviation was 14.5 cm, thus leading to a worst-case relative precision of 0.58%.

4. Discussion and FoM Analysis

Range-finding performance assessment typically involves a number of evaluation criteria and the eventual best approach for a given application may be suboptimal in other applications. In this paper, we focus on what we believe is the most important in possibly any application: repeatability error or, simply, precision. We therefore relate precision to other sensor design parameters in order to establish a general FoM for the evaluation and comparison of performance among different implementations.

As a benchmark for our paper, we compare our experimental results to previous TOF 3-D image sensor implementations [7]–[19], particularly those based on the so-called lock-in pixels [7] that have recently benefited from considerable interest [14]–[19]. One may therefore assume that those

approaches have already undergone some level of optimization and represents an appropriate benchmark for our newly proposed concept. Although our sensor architecture enables high SBR and is therefore suitable to operate under strong background illuminance, as shown in our experimental results, one may argue that immunity to background illuminance may not be mandatory in all applications. Indeed, precision has been so far reported in the literature under low or undisclosed background illuminance levels [14]–[19].

Recently, some FoM expressions have been introduced in [22] for the typical analog lock-in pixel architecture, wherein system-level parameters have been explicitly removed. Those expressions cannot be directly utilized to compare performance across different sensor architectures, particularly when inherently digital pixel sensors, e.g., [14] and [17], are included in the comparison. We therefore introduce an original expression, which, unlike in [22], also appropriately takes into account system-level parameters such as FOV and illumination power.

In the lock-in approach, distance is typically obtained by measuring the phase of a sinewave-modulated optical signal. An expression for the standard deviation error on the phase may be obtained by propagating the photon shot noise in the relationship between phase and the lock-in samples [23], thus leading to

$$\sigma_{\varphi} = \sqrt{\frac{b}{2a^2}} \tag{1}$$

where a and b are parameters related to the amplitude and offset of the sampled sinewave signal, respectively.

Assuming that the offset and the amplitude of the sinewave signal are ideally the same, i.e., $a = b$, and that the signal is sampled with four samples per period, the 1σ distance precision (σ_D) in [23] may be related to the integrated number of signal photo-electrons (N) and the distance range (R_D) by a simple expression, i.e.,

$$\sigma_D = \frac{1}{\sqrt{2}\pi}\frac{R_D}{\sqrt{N}}. \tag{2}$$

The scope of (2) is limited to the ideal case in which only signal photon shot noise is included, thus neglecting other effects such as shot noise from background photons, readout noise, and finite sampling bandwidth. We may therefore define a FoM expression as

$$\text{FoM} \propto \frac{R_D}{\sigma_D\sqrt{N}} \tag{3}$$

which can be used to compare performance in terms of precision among different implementations. The higher the FoM, the better the sensor precision under the constraints of a particular physical implementation. Assuming imaging formation by a standard imaging lens, light intensity on the image focal plane I_{FP} is proportional to the light intensity on the object plane (I_{OBJ}), which, in turn, may be expressed as function of R_D, the illumination power (P_{ILL}), the illumination horizontal (FOV_H), and illumination vertical (FOV_V) field of views as

$$I_{OBJ} = \frac{P_{ILL}}{4R_D^2\tan\left(\frac{\text{FOV}_H}{2}\right)\tan\left(\frac{\text{FOV}_V}{2}\right)}. \tag{4}$$

The absorbed optical power (P_{PX}) in a given imaging pixel is given by

$$P_{PX} = I_{FP}A_{PX} \propto I_{OBJ}A_{PX} \tag{5}$$

where A_{PX} is the pixel area. The number of detected photons in a pixel, in turn, is proportional to P_{PX} and inversely proportional to the sensor frame rate (F_R), i.e.,

$$N \propto \frac{P_{PX}}{F_R}. \tag{6}$$

By replacing (4), (5), and (6) into (3), while disregarding the factor 4 in the denominator of (4), we obtain a final expression for FoM as

$$\text{FoM} = \frac{R_D^2}{\sigma_D}\sqrt{\frac{F_R \tan\left(\frac{\text{FOV}_H}{2}\right)\tan\left(\frac{\text{FOV}_V}{2}\right)}{A_{PX}P_{ILL}}}. \tag{7}$$

In the derivation of FoM above, we focused on the lock-in-pixel approach in order to estimate relation (3). We believe that this relation is general to any diffused light implementation. Indeed, we have also verified that other approaches, including the so-called indirect TOF technique, e.g., [12], also lead to an expression whereby precision is proportional to distance range and inversely proportional to the square root of the number of detected photons, although the overall derivation was omitted in this paper. Table 1 summarizes the performance of our sensor and compares it to the recently published sensors in the state of the art [14], [15], [17]–[19]. As can be seen in Table 1, despite a stringent background illuminance condition, our sensor achieves a FoM considerably higher than that of the other sensors listed in the table. Note that since the derivation of FoM does not include a parameter for background illuminance, it does not penalize the remaining sensors of Table 1, which were characterized under low or undisclosed background illuminance. Our significantly higher FoM is believed to be enabled by the ability of our sensor to operate with a significantly smaller effective illumination duty cycle, when compared to the typical nearly 50% of duty cycle in the remaining approaches of Table 1, and by the advanced and nonlinear TCSPC processing [21].

5. Conclusion

A LIDAR system that takes advantage of a MEMS mirror and a single-photon imager has been proposed. The image sensor is fully synchronized with the MEMS mirror scanner in order to enable a high signal-to-background ratio. The separation of the transmitting and receiving optics enables the implementation of a large receiving aperture, while keeping the MEMS mirror size down to a minimum. Single-photon avalanche diodes have been utilized to detect individual photonic events with high timing resolution.

A proof-of-concept prototype operating in real-time has been designed and implemented. A MEMS mirror with a moving magnet configuration has been designed to work with only one pair of driving coils. The scanning amplitude has been characterized and proven to satisfy our system requirements of $\pm 4^\circ$ horizontally and $\pm 3^\circ$ vertically. The laser collimation optics has been designed aiming at compactness, ease of alignment, and small beam divergence. A unified collimation construction has been adopted for the three laser beams. A laser driver emitting laser pulses with 4-ns FWHM and a peak power of 40 W has been designed, manufactured and characterized. A single-photon image sensor chip with 256×64 pixels was designed in a high-voltage 0.18 μm CMOS technology. The overall assembled LIDAR system size was $19 \times 15 \times 8$ cm^3, which could be further miniaturized if, for instance, a folded optics construction were to be used.

Distance images have been acquired outdoors in order to qualitatively evaluate the imaging capabilities of our sensor. The shape of a pedestrian in the distance image, as well as road signs in the intensity image, could be readily recognized.

Ranging performance has been characterized quantitatively under several conditions of background light. The results showed that ambient background illuminance of up to 10 klx had a negligible impact on the sensor ranging performance. This was achieved by our proposed sensor architecture. The ranging performance was characterized for distances ranging up to 25 m. The distance precision was better than 14.5 cm throughout the distance range, thus leading to a relative precision of 0.58%. To the best of our knowledge, these results compare favorably to the state of the art.

Acknowledgment

The authors would like to thank M. Lany and R. S. Popovic of EPFL, as well as T. Kindo of Toyota Motor Corporation for their technical support with the design of the SPAD device.

TABLE 1

Comparison of performance to the recently published state of the art in CMOS

Parameter		Unit	Niclass, *et al.*, JSSC, 2009 [14]	Zach, *et al.*, JSSC, 2010 [15]	Walker, *et al.*, ISSCC, 2011 [17]	Stoppa, *et al.*, JSSC, 2011 [18]	Kim, *et al.*, ISSCC, 2012 [19]	**This Work**
Depth image resolution		pix.	60x48	16x16	128x96	80x60	480x270	**256x64**
Technology		-	0.35µm HV CMOS	0.6µm Bi CMOS	0.13µm imag. CMOS	0.18µm imag. CMOS	0.11µm imaging CMOS	**0.18µm HV CMOS**
Pixel area (A_{PX})		µm^2	85x85	125x 125	44.65x 44.65	10x10	14.6x14.6	**25x25**
Optical fill factor		%	<1	66	3.2	24	38.5	**13.9**
Photon detection efficiency or Quantum efficiency		%	3	Not stated	5	15[b]	Not stated	**3**
Illumination wavelength		nm	850	850	850	850	850	**870**
Illumination repetition rate or frequency		MHz	30	10	3.33	20	20	**0.6**
Illumination power (P_{ILL})		mW	800	900	50	80	Not stated	**75**
FOV_H x FOV_V		deg.	50x40	6x6[a]	40x40	8x6[a]	25x14[a]	**45x11**
Frame rate (F_R)		fps	22	16	20	5	11	**10**
Target reflectivity		-	White	White	White	White	White	**White**
Measured range (R_D)		m	2.4	3.2	2.4	6	4.5	**25**
Unambiguous distance range		m	5	15	45	7.5	7.5	**128**
Precision	σ_D	cm	3.8	<5	16	16	3.8	**14.5**
	Max. distance	m	2.4	3	2.4	6	4.5	**25**
	Background illuminance	klux	0.15	Not stated	0.11	Not stated	1.5	**10**
Non-line arity	Max. error	cm	11	5 (15)	0.5	4	4.2	**17**
	Max. distance	m	2.4	1.5	2.4	6	4.5	**25**
	Background illuminance	klux	0.15	100 (150)	0.11	Not stated	1.5	**10**
Figure of merit		(a.u.)	$3.9{\cdot}10^6$	$3.2{\cdot}10^5$	$5.9{\cdot}10^6$	$1.1{\cdot}10^7$	-	**$4.0{\cdot}10^8$**

[a] Calculated using published parameters as $FOV = 2 \cdot \tan^{-1}\left(\frac{h}{2f}\right)$, where f is the lens focal length and h is the pixel array width (H) and height (V). The FOV was not explicitly reported in the respective references.

[b] Converted from the published responsivity figure at the illumination wavelength.

References

[1] C. Niclass, K. Ito, M. Soga, H. Matsubara, I. Aoyagi, S. Kato, and M. Kagami, "Design and characterization of a 256 × 64-pixel single-photon imager in CMOS for a MEMS-based laser scanning time-of-flight sensor," *Opt. Exp.*, vol. 20, no. 11, pp. 11 863–11 881, May 2012.

[2] B. L. Stann, J. F. Dammann, M. M. Giza, W. B. Lawler, H. M. Nguyen, and L. C. Sadler, "MEMS-scanned ladar sensor for small ground robots," in *Proc. SPIE*, 2010, no. 7684, pp. 76841E-1–76841E-12.

[3] T. Sandner, M. Wildenhain, T. Klose, H. Schenk, S. Schwarzer, V. Hinkov, H. Höfler, and H. Wölfelschneider, "3D imaging using resonant large-aperture MEMS mirror arrays and laser distance measurement," in *Proc. IEEE/LEOS Opt. MEMS Nanophoton.*, 2008, pp. 78–79.

[4] T. Sandner, T. Grasshoff, M. Wildenhain, and H. Schenk, "Synchronized microscanner array for large aperture receiver optics of LIDAR systems," in *Proc. SPIE*, 2010, vol. 7594, p. 75940C.

[5] B. Schwarz, "LIDAR: Mapping the world in 3D," *Nat. Photon.*, vol. 4, no. 7, pp. 429–430, Jul. 2010.

[6] C. Niclass, M. Soga, H. Matsubara, and S. Kato, "A 100 m-range 10-frame/s 340× 96-pixel time-of-flight depth sensor in 0.18 μm CMOS," in *Proc. IEEE Eur. Solid-State Circuits Conf.*, 2011, pp. 107–110.

[7] R. Lange and P. Seitz, "Solid-state time-of-flight range camera," *IEEE J. Quantum Electron.*, vol. 37, no. 3, pp. 390–397, Mar. 2001.

[8] S. B. Gokturk, H. Yalcin, and C. Bamji, "A time-of-flight depth sensor - system description, issues and solutions," in *Proc. IEEE Comput. Soc. Conf. Comput. Vis. Pattern Recognit. Workshops*, 2004, p. 35.

[9] T. Oggier, B. Büttgen, F. Lustenberger, R. Becker, B. Rüegg, and A. Hodac, "SwissRanger SR3000 and first experiences based on miniaturized 3D-TOF cameras," in *Proc. 1st Range Imag. Res. Day*, 2005, pp. 97–108.

[10] C. Niclass, A. Rochas, P.-A. Besse, and E. Charbon, "Design and characterization of a CMOS 3-D image sensor based on single photon avalanche diodes," *IEEE J. Solid-State Circuits*, vol. 40, no. 9, pp. 1847–1854, Sep. 2005.

[11] T. Ushinaga, I. A. Halin, T. Sawada, S. Kawahito, M. Homma, and Y. Maeda, "A QVGA-size CMOS time-of-flight range image sensor with background light charge draining structure," in *Proc. SPIE*, 2006, vol. 6056, p. 605 604.

[12] G. Yahav, G. J. Iddan, and D. Mandelboum, "3D imaging camera for gaming application," in *Proc. IEEE Int. Conf. Consum. Electron.*, 2007, pp. 1–2.

[13] T. Ringbeck, "A 3D time of flight camera for object detection," in *Proc. 8th Conf. Opt. 3D Meas. Tech.*, Zurich, Switzerland, 2007.

[14] C. Niclass, C. Favi, T. Kluter, F. Monnier, and E. Charbon, "Single-photon synchronous detection," *IEEE J. Solid-State Circuits*, vol. 44, no. 7, pp. 1977–1989, Jul. 2009.

[15] G. Zach, M. Davidovic, and H. Zimmermann, "A 16 × 16 pixel distance sensor with in-pixel circuitry that tolerates 150 klx of ambient light," *IEEE J. Solid-State Circuits*, vol. 45, no. 7, pp. 1345–1353, Jul. 2010.

[16] S. Bellisai, F. Guerrieri, and S. Tisa, "3D ranging with a high speed imaging array," in *Proc. Conf. PRIME*, 2010, pp. 1–4.

[17] R. J. Walker, J. A. Richardson, and R. K. Henderson, "A 128 × 96 pixel event-driven phase-domain $\Delta\Sigma$-based fully digital 3D camera in 0.13 μm CMOS imaging technology," in *Proc. IEEE Int. Solid-State Circuits Conf., Dig. Tech. Papers*, 2011, pp. 410–412.

[18] D. Stoppa, N. Massari, L. Pancheri, M. Malfatti, M. Perenzoni, and L. Gonzo, "A range image sensor based on 10 μm lock-in pixels in 0.18 μm CMOS imaging technology," *IEEE J. Solid-State Circuits*, vol. 46, no. 1, pp. 248–258, Jan. 2011.

[19] S.-J. Kim, B. Kang, J. D. K. Kim, K. Lee, C.-Y. Kim, and K. Kim, "A 1920 × 1080 3.65 μm-pixel 2D/3D image sensor with split and binning pixel structure in 0.11 pm standard CMOS," in *Proc. IEEE Int. Solid-State Circuits Conf., Dig. Tech. Papers*, 2012, pp. 396–398.

[20] I. Aoyagi, K. Shimaoka, S. Kato, W. Makishi, Y. Kawai, S. Tanaka, T. Ono, M. Esashi, and K. Hane, "2-Axis MEMS scanner for a laser range finder," in *Proc. IEEE Int. Conf. Opt. MEMS Nanophoton.*, 2011, pp. 39–40.

[21] C. Niclass, M. Soga, and E. Charbon, "3D imaging based on single-photon detectors," in *Proc. 8th Conf. Opt. 3D Meas. Tech.*, Zurich, Switzerland, 2007, pp. 34–41.

[22] M. Perenzoni and D. Stoppa, "Figures of merit for indirect time-of-flight 3D cameras: Definition and experimental evaluation," *Remote Sens.*, vol. 3, no. 11, pp. 2461–2472, Nov. 2011.

[23] P. Seitz, "Quantum-noise limited distance resolution of optical range imaging techniques," *IEEE Trans. Circuits Syst. I, Reg. Papers*, vol. 55, no. 8, pp. 2368–2377, Sep. 2008.